Experimental axial-compressive behaviour of bare cold-formed-steel studs with semirigid-track and ideal-hinged boundary-conditions

Sohini Mishra [a,*], Ciaran McNally [a], Andrzej M. Wrzesien [b], Daniel P. McCrum [a]

[a] School of Civil Engineering, Newstead Building, University College Dublin, Dublin 4, Ireland
[b] School of Computing, Engineering & Physical Sciences, University of the West of Scotland, High Street, PA1 2BE Paisley, United Kingdom

ARTICLE INFO

ABSTRACT

Studs are the primary load-bearing components in cold-formed steel (CFS) wall panels, connected to tracks at both ends with self-tapping screws, forming a semirigid boundary condition (BCT). Most existing tests on the axial compressive behaviour of bare CFS studs are based on either theoretically-hinged (BCH) or fully-fixed boundary conditions. Previous researchers have employed BCT only on sheathed stud-wall panels. However, practicing engineers and current design codes, e.g., Eurocode 3, follow an all-steel design. Therefore, this research experimentally investigated bare-CFS-studs' axial compressive behaviour with BCT, considering, for the first time, the combined effect of the tracks' warping rigidity, stud-to-track gap, non-linear connection stiffness, and bare studs' various cross-sectional slenderness. Forty-two industry-standard lipped channel sections (studs) of five thicknesses (1.2-3 mm), three depths (75–125 mm), and two heights (1.2 & 1.5 m) were tested under static-concentric axial compressive loading with BCT. Another fourteen studs were tested with BCH, a comparator to BCT. Results demonstrated that the studs' global failure mechanisms were flexural-torsional in BCT instead of flexural in BCH. Studs' axial stiffness was two-phased in BCT due to the stud-to-track gap, compared to single-phased stiffness in BCH. >1.8 mm stud-to-track gap caused stud-to-track connections' failure and studs' sudden capacity reduction during gap closure. Studs achieved 1.22 times higher axial-compressive strength, 2.3 times more axial-shortening, 0.7 times lower axial stiffness, and 58% lower axial-compressive strain at the web-midheight under BCT-PhaseII than BCH. Tested strengths were compared with EC3 design strength, and an effective-length-factor of 0.65 was suggested for efficient design of studs with BCT.

1. Introduction

Cold-formed steel (CFS) panelised construction is becoming increasingly popular in the built environment for low-to-medium rise offsite residential, industrial, and commercial buildings [1] due to several advantages, such as improved construction speed, a higher strength-to-weight ratio, better energy efficiency, higher CFS recycling rate (about 66%), reduced maintenance & transportation costs, ease of handling, stacking, and reduced carbon emissions [2]. If designed and employed mindfully, CFS members can achieve more economical structures [2,3] compared to their hot-rolled steel (HRS) counterparts. CFS buildings typically employ load-bearing stud wall panels to withstand the gravity load and transfer it to the foundation as line loads [1]. Studs are the primary load-bearing vertical members in CFS wall panels connected to the tracks at the top and bottom (header and footer) with self-tapping (S/T) screws [4–6]. The track flanges provide a warping rigidity [7,8] to the stud ends. The S/T screws connecting the track and stud flanges exhibit a non-linear stiffness under various loading scenarios [1,9]. Furthermore, a gap between the stud and the track web exists in CFS wall panels as the stud initially makes contact with the track's rounded corner radius, not the web's flat portion [10]. With the combined effect of the tracks' warping rigidity, non-linear connection stiffness, and stud-to-track gap, the end condition for the studs in CFS wall panels is neither theoretically hinged nor fully fixed; rather, it forms a semirigid boundary condition. Due to this semirigid boundary condition, the behaviour of studs in the CFS stud wall panel is somewhere between a column (with full moment-fixity at the ends as in moment resisting frames) and a strut (with perfectly pinned boundary condition having zero moment fixity at the ends). Current design codes [11,12] often impede studs' economical and efficient design in CFS wall panels as they do not address the effect of the degree of fixity the track boundary condition provides [13,14], and the design solutions are

typically based on theoretical hinged boundary conditions. AISI S100–16 [12] mentions that the magnitude of the effective length factor (E_L) for designing columns should be based on the members' accurate boundary condition. AISI S100–16 [12] also recommends using either a conservative E_L of 1 for flexural buckling or conducting rational engineering analysis and testing to validate and employ a lower magnitude of E_L. Telue and Mahendran [13] reported a relationship between the flexural rigidity ratio of the track to stud and the E_L of bare CFS studs that undergo two distinct failure mechanisms: local and global buckling based on testing two full-scale bare CFS wall panels consisting of two different depths of studs: 75 mm and 200 mm. However, the effect of the studs' other cross-sectional slenderness, which could instigate complex buckling mode interactions in real-world track boundary condition scenarios, was not investigated. All existing experimental investigations [15–18] on individual bare CFS studs employed either conventional hinge or fixed boundary conditions to investigate the effect of local-flexural buckling mode interactions affecting the ultimate axial strength of the CFS studs. However, such theoretical conditions rarely exist in reality. More recently, Rajkannu and Jaychandran [19] suggested a correction factor to be applied to the direct strength method (DSM) column strength curves to consider the effect of warping fixity on the flexural-torsional buckling strength of axially loaded CFS-lipped channel sections. However, the fixed warping condition in their experiments [19] was created by directly welding the specimen to an end plate, which significantly differed from the studs' real-world, semirigid track boundary condition in CFS wall panels. Ye et al. [20] and others [8,21,22] experimentally investigated sheathed stud-wall panels with a track boundary condition to find out how the composite action of sheathing influences the stability and strength of sheathed CFS stud wall panels. These researchers maintained a constant cross-section of the stud and tracks and varied the sheathing type/configuration. The sheathing increased the axial capacity of the studs by increasing their resistance against local, global, and distortional buckling [1,22]. However, the sheathing did not influence the studs' axial stiffness compared to the axial stiffness of bare studs (of the same cross-section as the sheathed one) with track boundary conditions [7]. However, Lawson et al. [8] highlighted that the contribution of sheathing to the load-bearing capacity of the studs should not be overly relied upon as they may be damaged or replaced at some stage. Furthermore, practitioners and some design codes, such as the Eurocode 3 [11], do not include the composite action of the sheathing but consider an 'all-steel' design approach [1]. In addition, no previous researchers have investigated the effect of the stud-to-track gap on the axial compressive performance of bare CFS studs. Only LaBoube and Findlay [10] have investigated the stud-to-track gap, amongst other parameters, for sheathed CFS stud wall panels to investigate the effect of the gap particularly on the stud-to-track connection strength and the aesthetics of the sheathing. The various diameter of screws used at the stud-to-track connections were: No 8 and No 10, as per industry standard. Even with sheathing, the stud-to-track connections underwent shear failure for a gap of >2 mm. To avoid such connection failure, Vieira Jr. et al. [8] eliminated the gap to the maximum extent possible while investigating the axial compressive strength of sheathed stud wall panels. However, eliminating the stud-to-track gap does not match the 'real-life' stud-to-track connecting arrangement.

From the literature, it is evident that no existing research has investigated the bare CFS studs' ultimate axial compressive strength, stiffness, load-deformation response, and failure mechanism along the entire load equilibrium path whilst considering the combined effect of the tracks' warping rigidity, non-linear connection performance, stud-to-track gap, and the studs' various cross-sectional slenderness, with real-world track boundary conditions. The common engineering practice is to design the studs in CFS wall panels with an ideal hinged boundary condition. Hence, a comparison of the influence of real-world track boundary conditions with that of a theoretical hinged boundary condition is necessary to obtain more profound insight into the variation

in the studs' axial compressive performance due to changes in boundary conditions from theoretical to semirigid in reality. This research aims to address this existing gap in the literature by experimentally investigating the axial compressive performance of industry-standard bare CFS studs with various cross-sectional and non-dimensional slendernesses under a semirigid track boundary condition (referred to as BCT, i.e., Boundary Condition Track) as employed in reality and a theoretical hinge boundary condition (referred to as BCH, i.e., Boundary Condition Hinge). For the first time, the individual bare CFS studs' axial compressive performance, strength, stiffness behaviour, and failure mechanism are compared experimentally under BCT and BCH. The combined effects of the tracks' warping rigidity, stud-to-track gap, non-linear connection failure mechanism, and studs' various cross-sectional slendernesses are investigated. The influence of measured geometric imperfections' distribution axial compressive strains is studied in detail. In addition, to account for the effect of warping rigidity provided by the tracks, the Eurocode 3 [11] effective width method (EWM) of design is evaluated, and possible modifications are suggested to predict the studs' axial compressive strength in BCT. These findings will enable the more efficient design of CFS studs with semirigid track boundary conditions under axial compressive loading.

2. Stud testing program

Commercially available, CFS-lipped channel sections of three different depths (75, 100, and 125 mm) and five different thicknesses (1.0, 1.2, 1.3, 2.0, and 3.0 mm) were tested with 1.2 m and 1.5 m lengths representing the effective length of the studs usually employed in the CFS wall panels with noggins at mid-height (to provide lateral restraint about the studs' minor centroidal axis); i.e. half the typical CFS panel heights of 2.4 m and 3.0 m. The primary purpose of this study is to investigate the effect of the semirigid-track-boundary condition on the studs' axial-compressive performance, for which it was essential to test the columns with both header and footer track sections. Due to the laboratory constraint of the strong reaction frame, the half-panel height was chosen as the stud height, as it was considered the most practically appropriate length of studs to be used to assess the effect of the track-boundary condition. A similar concept was followed by Ye et al. [14] for testing bare CFS columns under perfectly pinned boundary conditions. The two different boundary conditions investigated were:

1. Semirigid track boundary condition (BCT): The studs were connected to 300 mm long corresponding tracks (refer to Table 2) on both ends with self-tapping (S/T) screws based on an industry standard arrangement. Various industry standard S/T screws, such as No 6, No 8, No 10, and No 12, have been used by previous researchers [7,10,22] at the stud-to-track connection. This research used industry standard No 12 (5.5 mm dia) S/T screw at the stud-to-track connections. The screws were connected at the intersection point of the minor centroidal axis of the stud flange and the center of the track flange at the track's mid-length to ensure concentric load application.

2. Hinged boundary condition (BCH): A theoretical boundary condition of the studs at both ends used as a comparator to BCT. Fifty-six studs were tested—four samples of each stud section, three with BCT and one with BCH.

Fig. 1 shows the two boundary conditions, BCT and BCH. Table 1 shows the stud test program. Specimen IDs a, b, c, and d indicate repeat tests. Section 2.1 details the experimental setup, arrangements of the two boundary conditions, and experimental instrumentation. For details of the specimen cross-sections, refer to Section 2.3.

2.1. Experimental setup and instrumentation

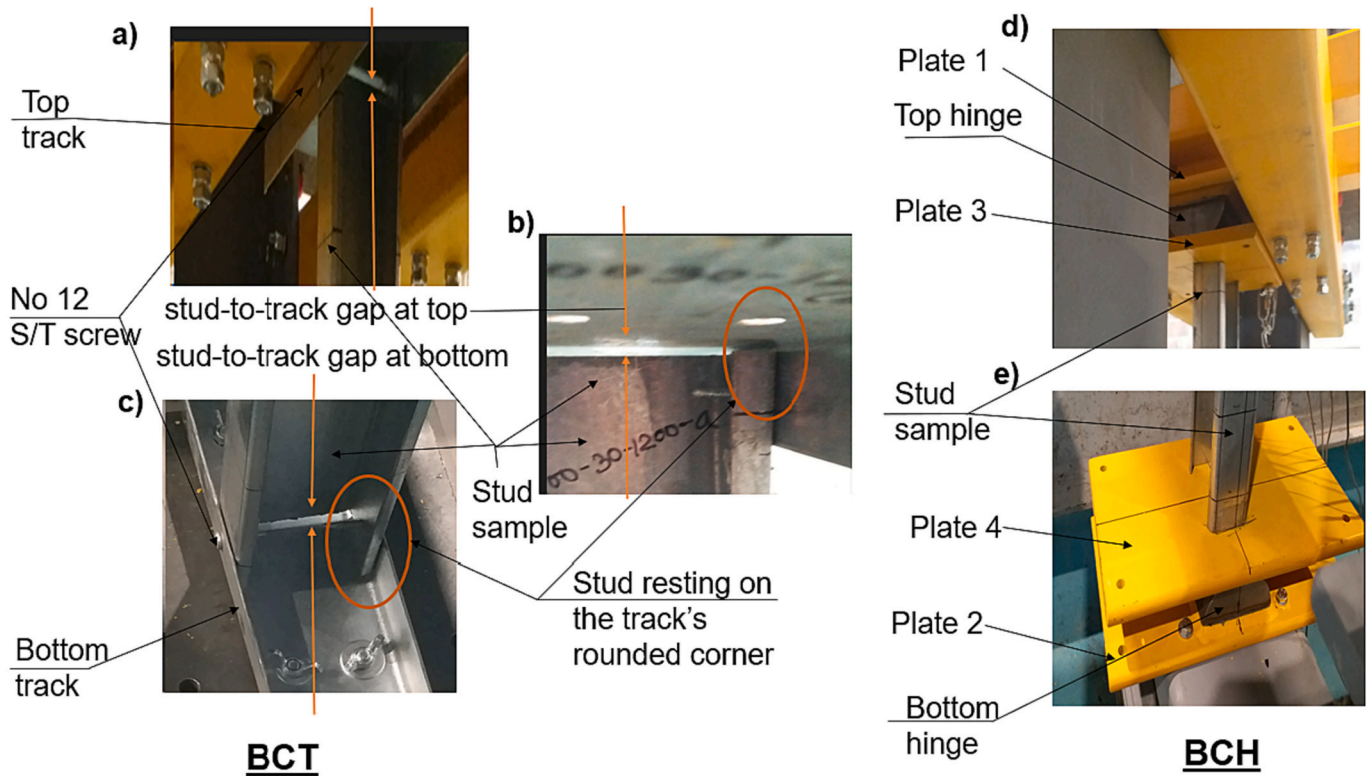The schematic diagram and picture of the experimental setup are

Fig. 1. Boundary conditions: a), b) & c) semirigid track (BCT) – top (a,b) & bottom (c), respectively; d) & e) hinged with no track (BCH) - top & bottom, respectively.

Table 1
Experimental program for CFS bare studs.

Test No	Specimen ID	Boundary Condition	Strain Gauged (Y/N)	Test No	Specimen ID	Boundary Condition	Strain Gauged (Y/N)
1	S75-12-1200-a	BCT	Y	29	S100–30-1500-c	BCT	N
2	S75-12-1200-c	BCT	N	30	S100–30-1500-d	BCT	N
3	S75-12-1200-d	BCT	N	31	S125–13-1200-a	BCT	Y
4	S75-12-1500-a	BCT	Y	32	S125–13-1200-c	BCT	N
5	S75-12-1500-c	BCT	N	33	S125–13-1200-d	BCT	Y
6	S75-12-1500-d	BCT	N	34	S125–13-1500-a	BCT	Y
7	S75-15-1200-a	BCT	Y	35	S125–13-1500-c	BCT	N
8#	S75-15-1200-c	#	#	36	S125–13-1500-d	BCT	N
9	S75-15-1200-d	BCT	N	37	S125–20-1200-a	BCT	Y
10	S75-15-1500-a	BCT	Y	38	S125–20-1200-c	BCT	N
11#	S75-15-1500-c	#	#	39	S125–20-1200-d	BCT	N
12	S75-15-1500-d	BCT	N	40	S125–20-1500-a	BCT	Y
13	S100–12-1200-a	BCT	Y	41	S125–20-1500-c	BCT	N
14	S100–12-1200-c	BCT	N	42	S125–20-1500-d	BCT	N
15#	S100–12-1200-d	#	#	43	S75-12-1200-b	BCH	Y
16	S100–12-1500-a	BCT	Y	44	S75-15-1200-b	BCH	Y
17	S100–12-1500-c	BCT	N	45	S100–12-1200-b	BCH	Y
18	S100–12-1500-d	BCT	N	46	S100–20-1200-b	BCH	Y
19	S100–20-1200-a	BCT	Y	47	S100–30-1200-b	BCH	Y
20	S100–20-1200-c	BCT	N	48	S125–13-1200-b	BCH	Y
21	S100–20-1200-d	BCT	N	49	S125–20-1200-b	BCH	Y
22	S100–20-1500-a	BCT	Y	50	S75-12-1500-b	BCH	Y
23	S100–20-1500-c	BCT	N	51	S75-15-1500-b	BCH	Y
24	S100–20-1500-d	BCT	N	52	S100–12-1500-b	BCH	Y
25	S100–30-1200-a	BCT	Y	53	S100–20-1500-b	BCH	Y
26	S100–30-1200-c	BCT	N	54	S100–30-1500-b	BCH	Y
27	S100–30-1200-d	BCT	N	55	S125–13-1500-b	BCH	Y
28	S100–30-1500-a	BCT	Y	56	S125–20-1500-b	BCH	Y

The test data corrupted for test no 8,11&15 due to power disruption in the lab.

shown in Fig. 2. The test setup consisted of two strong reaction frames 6.5 m long, 2.15 m high, and transverse spacing of 1.2 m (Fig. 2a). An Instron servo-hydraulic actuator, with a static compressive capacity of 266 kN and a stroke of 250 mm (± 125 mm), was mounted at the midspan on the reaction frame. On the reaction frame, a pair of strong

supporting columns were placed precisely below the actuator supporting point to prevent deflection of the support (reaction frame beam) at the load application point. A UC 254x254x73 beam (Fig. 2a) spanned between the two reaction frames to support the 1.5 m long stud at the bottom. For the 1.2 m long samples, a UB 305x165x54 section (Fig. 2b)
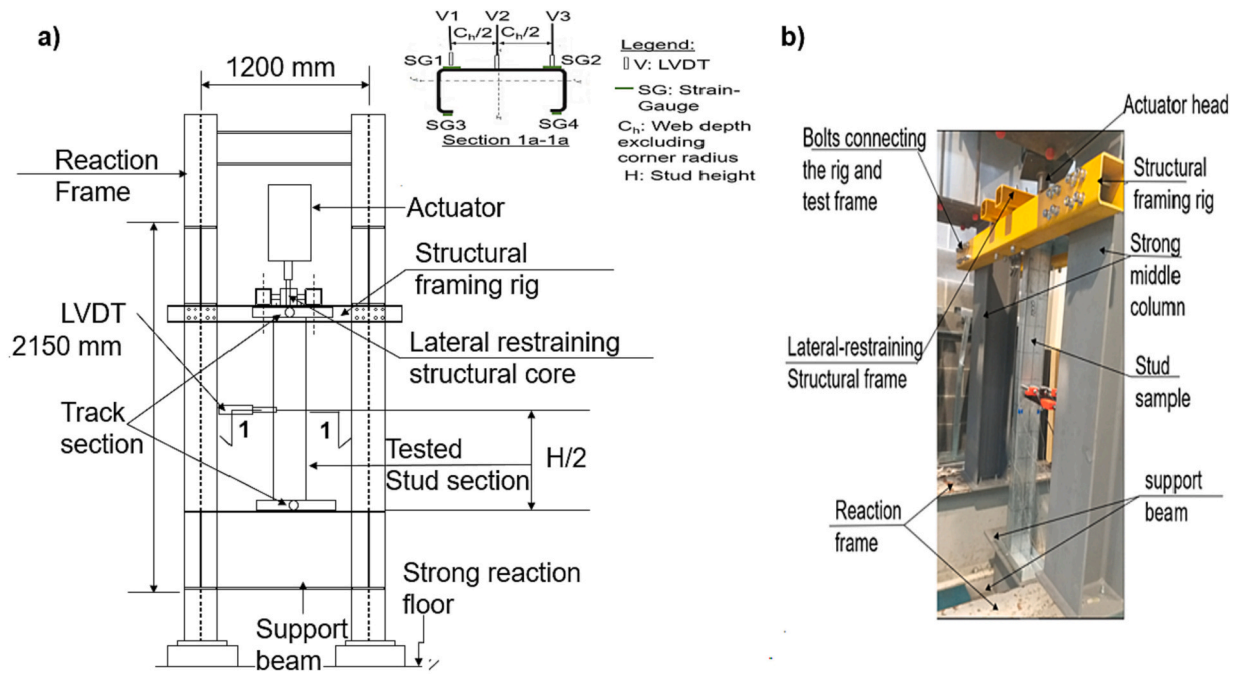
Fig. 2. a) Schematic diagram of the test setup with instrumentation (Table 1); b) photograph of test setup for 1.2 m height stud sample S125–20-1200-a.

was bolted on top of the bottom support beam as a packer. At the top of each stud, a structural framing rig with a lateral restraining structural frame was specifically designed to support, connect, and prevent any lateral displacement of the top of the studs in BCT and BCH. The actuator head applied the load to the sample through a 200 mm square 16 mm thick HRS loading plate. In BCT (Fig. 1a&b), the stud-track assembly at the top and bottom was connected to the loading plate and bottom support beam flange with four M8 (Gr. 8.8) bolts. The BCH (Fig. 1c&d) was fabricated with four 16 mm thick loading plate sets. A 100 mm diameter solid half-round bar was welded to plates 1 & 2 at the top and bottom to allow free rotation of plates 3 & 4 around the longitudinal axis of the half-round bar. The lateral movement of the sample on the loading plates in BCH was prevented by friction, as was also followed by [17,18]. Fig. 2a and section 1–1 shows the instrumentation applied to each specimen. A linear variable differential transducer (LVDT), marked as V4, was connected internally with the actuator head to measure the

studs' axial shortening. At the mid-height, three more LVDTs, V1, V2, and V3, were attached to the sample, as shown in Fig. 2 a), section 1–1, to measure the samples' out-of-plane displacements. One sample of each section and each height in BCT and BCH were instrumented with strain gauges at the mid-height as per the arrangement shown in Fig. 2a, section 1–1.

2.2. Loading details

The studs were tested under concentric, monotonic, displacement-controlled axial compressive loading, applied at a consistent strain rate of 1.95×10^{-6}/s, implying that the displacement rate varied between 0.14 mm/min for 1.2 m long and 0.18 mm/min for 1.5 m long specimens. Each test was halted for 2/3 min, at or near the peak load, to determine the load's lower bound 'static' value, independent of strain-rate dependent effects following [16,23].

Table 2
Out-to-out cross-section dimensions of studs and tracks.

Section type	Specimen	Statistic	h (mm)	b1 (mm)	b2 (mm)	c1 (mm)	c2 (mm)	r (mm)	t (mm)
Stud	S75–12	*Mean*	73.9	42.4	42.7	8.4	7.9	1.8	1.18
		COV	0.001	0.008	0.008	0.048	0.056	0.000	0.009
	S75–15	*Mean*	75.7	42.6	42.9	8.4	8.1	2.2	1.48
		COV	0.002	0.007	0.005	0.035	0.049	0.000	0.018
	S100–12	*Mean*	101.7	49.8	49.9	9.6	9.7	1.7	1.21
		COV	0.002	0.005	0.011	0.023	0.032	0.045	0.004
	S100–20	*Mean*	99.4	51.2	50.9	12.9	12.6	3.2	2.01
		COV	0.002	0.021	0.025	0.087	0.081	0.015	0.002
	S100–30	*Mean*	100.3	50.7	50.7	19.5	17.2	4.3	3.04
		COV	0.001	0.016	0.015	0.063	0.077	0.000	0.007
	S125–13	*Mean*	124.5	52.2	52.3	19.9	18.5	2.3	1.24
		COV	0.001	0.010	0.012	0.101	0.098	0.020	0.008
	S125–20	*Mean*	125.2	51.8	52.0	18.4	18.04	3.2	1.99
		COV	0.000	0.009	0.008	0.043	0.037	0.000	0.012
Track	T79–15	*Mean*	80.3	37.2	37.1	–	–	2.4	1.56
		COV	0.007	0.005	0.005	–	–	0.037	0.046
	T104–20	*Mean*	106.5	55.8	54.9	–	–	3.2	2.04
		COV	0.006	0.031	0.013	–	–	0.014	0.018
	T129–20	*Mean*	130.8	42.9	42.8	–	–	3.1	2.02
		COV	0.005	0.010	0.010	–	–	0.025	0.024

2.3. Cross-section geometries, studs' cross-sectional classification, and non-dimensional slenderness

The average cross-section (out-to-out) dimensions of the tested studs and tracks are provided in Table 2, where h is the overall cross-sectional depth, b is the cross-sectional width, c is the depth of the lip, r is the internal corner radius, and t is the galvanized cross-sectional thickness. The base metal thicknesses are provided in Table 4. Three measurements were taken at the two ends and mid-length for the studs and tracks to account for the cross-section variation. In the symbol definitions of the specimens, S indicates studs, and T indicates tracks. The overall depth of the stud and tracks in mm is indicated after S and T, respectively. The last number indicates the specimens' galvanized thickness multiplied by 10.

The average cross-sectional and non-dimensional slenderness of each stud cross-section are presented in Table 3 and are defined as c_h/t: slenderness of the web or cross-sectional slenderness; $\lambda_{1.2}$, $\lambda_{1.5}$: non-dimensional slenderness ratio for the studs' effective length 1.2 m and 1.5 m, respectively expressed as; $\lambda = \sqrt{\frac{A_{eff}f_{yb}}{N_{cr}}}$ where, A_{eff} = Effective cross-sectional area in compression; f_{yb} = Proof strength, $\sigma_{0.2\%}$(Table 4); N_{cr} = Elastic critical force for the relevant buckling mode, as per clause 6.2, EC3 [11]. Table 3 shows that the c_h/t of all of the studs exceeds 42ε ($c_h/t > 42 \varepsilon$) except S10030; hence, the studs are classified as Class 4 sections as per EN 1993-1-1, Table 5.2 [24]. The c_h/t of S10030 stud is $< 38 \varepsilon$ (29.6); hence, classified as class 2 as per [24].

2.4. Coupon tests

The coupon tests were performed following the procedure described in [25]. The tensile coupons were grouped according to their thicknesses (five different thicknesses for the studs). Four coupons were longitudinally cut from the flat part (center) of the web and flange for each base metal thickness. A summary of the average mechanical properties of the coupons is presented in Table 4. The engineering stress-strain curves for each base metal thickness are shown in Fig. 3. The steel grades, presented in Table 4, were assigned based on the coupon test data, following the nominal values provided in Table 8 of BS EN 10346: 2015 [26].

Table 4 shows that the tested CFS sections have slightly higher measured material strengths compared to the minimum requirements as per the grades. The percentage difference between the measured and nominal proof strength ($\sigma_{0.2\%}$) for various coupons of respective steel grades varied between a minimum of 2% for 1.25 mm thick coupons to a maximum of 15% for 1.5 mm thick coupons, with an overall average difference of 7%. The percentage difference between the measured and nominal ultimate strength (σ_u) for various coupons of respective steel grades varied between a minimum of 1% for 2 mm thick coupons to a maximum of 22% for 3 mm thick coupons, with an overall average difference of 10%. The difference in the maximum strain amongst different coupons, depicted in Fig. 3, is due to the difference in the steel

grades of the coupons, as presented in Table 4. The higher the grade of steel, the less ductile the steel is, as shown in Fig. 3.

2.5. Imperfection measurements

The similarity of geometrical imperfections' distribution and competing buckling mode shapes can cause the lowest member strength [27]. Hence, the imperfections of each stud specimen were recorded before testing by employing the traditional manual measurement method with a digital gauge mounted on a precision rail, as shown in Fig. 4a. The measurements were taken at six different lines across the member cross-section (Fig. 4b). The web imperfections were measured at lines C, D, and E at 5 mm intervals. The flange imperfections were measured at lines A, B, F, and G at 100 mm intervals along the specimen length. Imperfections are calculated as per [7,18]. The average imperfection for each section size (the average of the maximum measured imperfection of each sample type) was normalized to the base metal thickness, t (for cross-sectional imperfection), and member length, L (for global imperfection) as per [28,29], and is provided in Table 5. The local and distortional imperfections have been denoted as type 1 - (d1/t) and type 2 - (d2/t), respectively. Fig. 5a to d shows an example of typical studs' distribution of measured geometrical imperfections indicating the local and global buckling mode-shapes.

2.6. Calculation of initial eccentricity

The out-of-plane eccentricity triggers cross-sectional instability and the interaction of buckling modes, causing a reduction in member strength [16,18]. In this study, the initial out-of-plane eccentricity was calculated at the studs' mid-height ($e_{0, mid}$) and end ($e_{0, end}$) using the strain gauge, LVDT data, and measured global imperfections at the mid-height ($g_{0, mid}$) as per [16,18]. The studs' $e_{0, end}$ are presented in Tables 6 and 7. The initial eccentricities are small, <2 mm, in most samples except for S100–12-1200-b, S100–20-1200-b, and S100–20-1500-b due to their higher imperfections. Since most samples had low initial eccentricities, it can be considered that any non-strain gauged samples had similar initial eccentricities.

2.7. The gap between stud and track

Based on the accepted industry practice, ASTM [30] sets a stud-to-track gap limit of 3 mm for axial load-bearing studs. In this study, the approximate maximum gap was measured with a micrometer at the top and bottom for every sample (see Table 6). The gap was not uniform across the stud web due to the studs' imperfect geometry. For most specimens, the measured maximum gap was <3 mm, except for some specimens S100–30-1500-c-top, S100–30-1200-a-bot, etc., where the gap was more due to higher geometric imperfections.

3. Overall test results

The results of the axial compressive tests under BCT and BCH are discussed herein.

3.1. Test results for BCT

In BC1, three distinct phases of loading were observed: Phase I: During the closure of the initial gap between the stud and track, Phase II: Post-gap-closing up to the peak load, and Phase III: Post-peak behaviour. Table 6 presents the peak load (P_{uBCT}) and the failure mechanism of the tested studs.

3.1.1. Phase I (BCT): Initial closure of the gap between the stud and track and related connection behaviour

At the initial loading phase, the gap between the stud and track (Fig. 6 a) closed gradually, with or without the failure of the self-tapping

Table 3
The studs' cross-sectional classification and non-dimensional slenderness.

Cross-section	c_h/t	f_y (MPa)	$\varepsilon = \sqrt{\frac{235}{f_y}}$	42ε	Section classification	$\lambda_{1.2}$	$\lambda_{1.5}$
S7512	57.6	366.2	0.80	33.6	Class4	1.35	1.62
S7515	46.3	518.9	0.67	28.3	Class4	1.41	1.74
S10012	79.4	366.2	0.80	33.6	Class4	0.97	1.2
S10020	44.2	439.7	0.73	30.7	Class4	1.22	1.48
S10030	28.1	382.3	0.78	32.9	Class2	1.03	1.24
S12513	95.2	458.6	0.72	30.1	Class4	0.74	0.93
S12520	57.8	439.7	0.73	30.7	Class4	0.97	1.20

c_h - web depth (corner radius excluded); t - base metal thickness.

Table 4
Summary of average measured mechanical properties of the coupons.

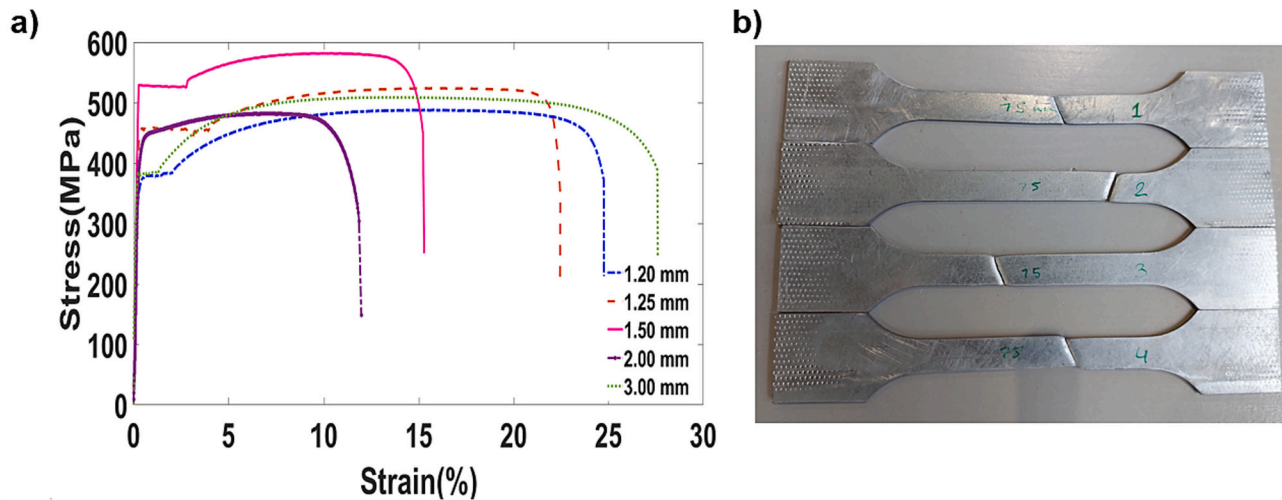| Coupon thickness (including galvanization)	Base metal thickness	Young's Modulus, E	Proof strength, $\sigma_{0.2\%}$	Ultimate strength, σ_u	strain at σ_u, ε_u	Grade of steel as per BS EN 10346:2015, Table 8 [26]	Nominal proof strength, R_{p02} [26]	Nominal ultimate strength, R_m [26]
(mm)	(mm)	(MPa)	(MPa)	(MPa)	(%)		(MPa)	(MPa)
1.2	1.18	179,223.7	366.2	474.9	16	S350GD	350	420
1.25	1.22	210,598.8	458.6	526.9	16	S450GD	450	510
1.5	1.46	216,370.5	518.9	575.4	11	S450GD	450	510
2	1.98	181,365	439.7	486.6	8	S420GD	420	480
3	3.00	210,340.8	382.3	511.1	13	S350GD	350	420

Fig. 3. a) Engineering stress-strain curves of tested coupon's first sample; and b) 2 mm thick CFS coupon specimen after conducting the tensile test.
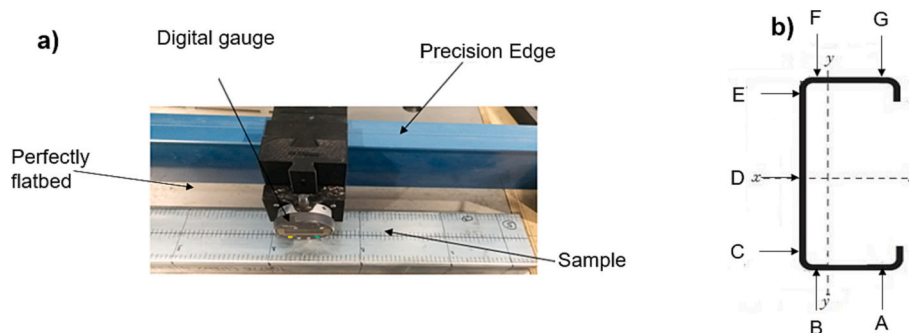

Fig. 4. a) Experimental setup for imperfection measurements; and b) cross-section imperfection measurement locations.

screws at the stud-to-track connections. In general, the connection failure occurred whenever the gap was >1.8 mm. A similar observation was reported by [10] for sheathed studs, where the connections failed for a gap >2 mm. For most S75 studs, only the bottom connections failed; in contrast, for the S75-12-1500-d & S75-15-1500-d studs, all four connecting S/T screws failed Fig. 6b). No connection failure occurred for most S100–12 and S125–13 studs (Fig. 6f). The bottom connections failed on both sides for most thicker gauges (2 mm & 3 mm thickness) studs. For the thinner gauge 1.2, 1.3, and 1.5 mm studs, generally, the screws underwent a ductile tilting failure (Fig. 6b), with no drop in the load during the closure of the gap except for S100–12-1500-a (Fig. 6 d), where initially screw tilting followed by a screw shear failure accrued. All the thicker 2 mm and 3 mm gauge studs experienced a brittle screw-head shear failure (Fig. 6e). An abrupt drop in stud capacity accompanied the connections' brittle failure (Fig. 6g & h). The load sometimes dropped more than once during the gap closure due to each screw

failure. Only in S75 studs a local deformation of the tracks was observed during the gap's closure, as the track was also 1.5 mm thick (Fig. 6c). The tracks were 2 mm thick for all other studs, which underwent no local deformation during the gap's closure (Fig. 6d & e). In Phase I, the studs' axial stiffness (k1, $_{BCT}$) was dominated by the stud-to-track gap and connections' non-linear shear stiffness. Fig. 6 shows various connection failure mechanisms in loading Phase I.

3.1.2. Phase II (BCT): The studs' performance post-gap closing and failure mechanism

After the top and bottom stud-to-track gaps were closed, the studs' ends fully beared on the track web. In Phase II, the studs demonstrated a2 higher axial stiffness, k2, $_{BCT}$, than in Phase I (k1, $_{BCT}$). k2, $_{BCT}$ represented the axial stiffness of the stud up to the ultimate load. The two different stiffnesses of the load-deformation curve can be seen in Fig. 7 and are reported in Table 6. The magnitude of k1, $_{BCT}$, and k2, $_{BCT}$ are

Table 5
Studs' average measured global, local and distorsional imperfections.

| Speci-men	Len-gth (mm)	No of sam-ple	Twist, dφ (deg)		d_b (L/bow)		dc (L/ camber)		d1/t		d2/t	
			Me-an	COV	Mean	COV	Mean	COV	Me-an	COV	Mean	COV
S75–12	1200	4	2.7	0.24	978.2	0.02	682.3	0.28	0.29	0.29	0.97	0.27
S75–15	1200	4	2.2	0.17	867.5	0.14	641.8	0.26	0.29	0.28	0.94	0.25
S100–12	1200	4	2.9	0.06	1127.8	0.59	932.0	0.52	1.06	0.34	1.04	0.59
S100–20	1200	4	0.9	0.23	1260.5	0.32	612.3	0.07	0.30	0.33	0.59	0.08
S100–30	1200	4	1.4	0.22	1087.3	0.95	481.3	0.17	0.26	0.9	0.49	0.16
S125–13	1200	4	0.7	0.35	847.4	0.33	400.1	0.09	0.90	0.56	1.41	0.2
S125–20	1200	4	2.2	0.23	892.0	0.83	498.9	0.11	0.41	0.32	0.65	0.08
S75–12	1500	4	3.9	0.12	584.2	0.31	816.1	0.25	0.28	0.28	1.06	0.09
S75–15	1500	4	2.4	0.18	537.9	0.22	676.2	0.06	0.26	0.5	1.06	0.09
S100–12	1500	4	2.6	0.09	1722.9	0.55	582.3	0.02	0.68	0.46	2.22	0.09
S100–20	1500	4	0.8	0.38	889.5	0.27	752.6	0.22	0.23	0.38	0.67	0.21
S100–30	1500	4	1.6	0.28	662.9	0.64	658.4	0.24	0.21	0.06	0.48	0.33
S125–13	1500	4	1.2	0.3	1031.0	0.73	476.9	0.15	0.71	0.40	1.50	0.20
S125–20	1500	4	1.9	0.08	895.9	0.65	618.9	0.09	0.42	0.17	0.66	0.08
Total average			1.96		956.1		630.7		0.45		0.98	
COV			0.47		0.31		0.23		0.61		0.49	
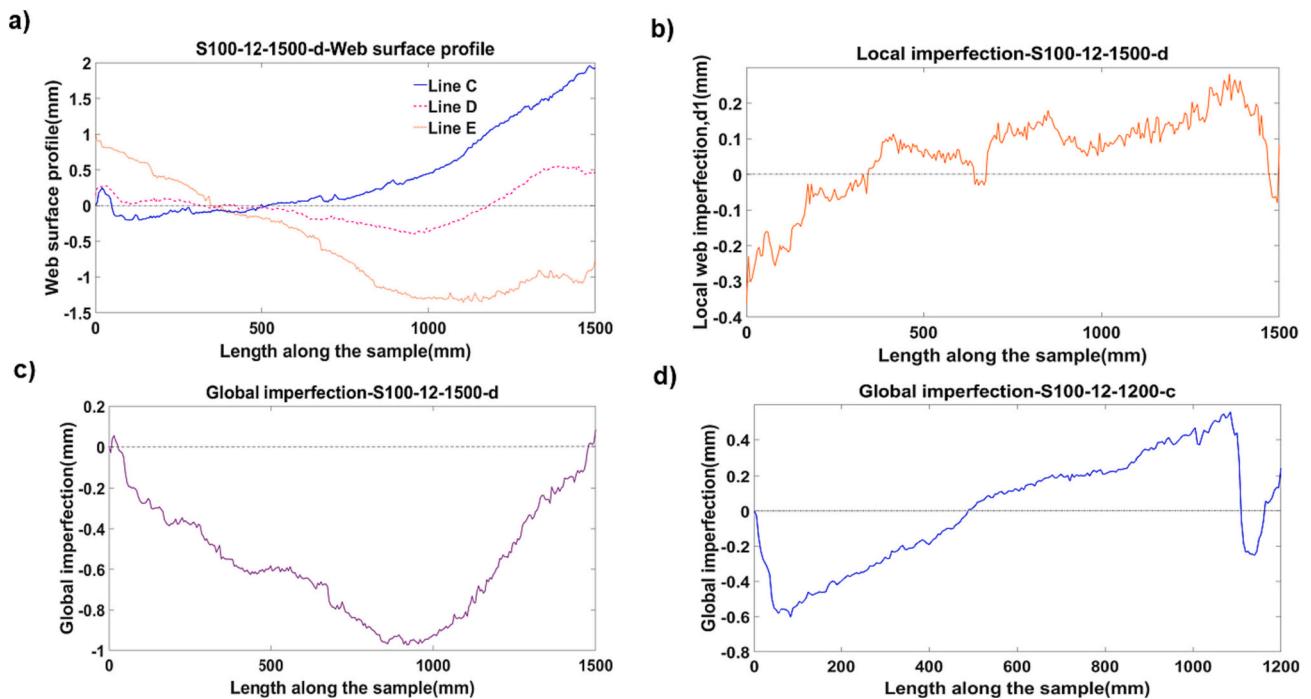
Fig. 5. a) Web surface imperfection profile for S100–12-1500-d specimen, b) type 1 (d1) local imperfection for S100–12-1500-d specimen, c) global imperfection (flexural) for S100–12-1500-d specimen, and d) global imperfection (flexural torsional type) for S100–12-1200-c specimen.

obtained from the slope of the load-axial shortening curve in Phase I & II. In BCT, the studs' predominant global failure mechanism was flexural-torsional. Table 6 shows that the studs experienced five different combinations of global and cross-sectional buckling failure mechanisms: 1) $D^a + FT^b + L^c$: Interaction of flexural torsional (FT^b) with distortional (D^a) and local (L^c) buckling, 2) $D^a + FT^b$: Interaction of flexural torsional (FT^b) with distortional (D^a) buckling, 3) $FT^b + L^c$: Interaction of flexural torsional (FT^b) with local (L^c) buckling 4) $L^c + D^a + F^d$: Interaction of local (L^c), distortional (D^a), and flexural (F^d) buckling. 5) $F^d + FT^b + L^c$: Interaction of flexural torsional (FT^b) with local (L^c) and flexural buckling (F^d) about the minor centroidal axis.

In BCT, the warping rigidity of the tracks triggered the global flexural-torsional failure mode of the studs. The coupling of different buckling modes started at the initial loading stage and evolved as the loading progressed throughout the equilibrium path. A summary of each cross-section performance, buckling mode interactions, and failure mechanisms in BCT, Phase II are discussed herein.

Most S75 studs experienced a sudden $D^a + FT^b + L^c$ failure. The local web (at studs' mid-height) and distortional buckling (at one-quarter height from the top of stud) of the web to flange junction initiated at 40–60% of the peak load. Apart from the effect of the tracks' warping rigidity, the global flexural-torsional mechanism was also influenced by the flexural-torsional types imperfection distribution profiles of the S75 studs.

Most S100 studs experienced interaction of flexural-torsional buckling with local and/or distortional buckling modes, causing a sudden failure. A flexural-flexural torsional mode (global-global) interaction was observed in all the 1.5 m long S100–30 studs as their global imperfection distributions were flexural type. The local web buckling initiated between 55 and 70%, 50–60%, and 85% of the peak load in S100–12, S100–20, and S100–30 studs, respectively. The distortional buckling of the web-to-flange junction initiated at 50–60% and 80–90% of the peak load in S100–12 and S100–20 studs, respectively.

S125 studs had the most slender webs amongst all the tested studs;

Table 6
Experimental performance, failure mechanism, peak load, and post-peak behaviour of the studs in BCT.

Test no/ Specimen ID	Measured Initial eccentricity $e_{0,end}$ (mm)	Stud-to-track gap at top; bottom (mm)	Phase I Connection (S/T) screw failure type (visual observation)	Axial Stiffness k1 (kN/mm)	Phase II Axial stiffness $k2,_{BCT}$ (kN/mm)	Tested peak load, P_{uBCT} (kN)	Failure mechanism	Total axial shortening at the peak load, V_{BCT} (mm)	Phase III Stud Failure type (visual observation)	Post-peak capacity reduction (% of ultimate capacity); reduced force (kN)
1/S75-12-1200-a	−1.96	2.9; 1.1	tilting	3.8	5.9	33.7	D^a+FT^b + L^c	7.6	Brittle	52.2%; 16.1
2/S75-12-1200-c	–	2.8; 0.98	tilting	1.3	6.0	35.4	D^a+FT^b + L^c	7.7	Brittle	60.5%; 13.9
3/S75-12-1200-d	–	2.5; 1.24	tilting	2.9	6.1	38.9	D^a+FT^b	8.0	Brittle	89.5%; 4.1
4/S75-12-1500-a	−2.39	2.3; 2.2	tilting	1.5	5.3	33.3	D^a+FT^b + L^c	8.4	Brittle	61.9%; 12.7
5/S75-12-1500-c	–	4.1; 4.0	tilting	2.1	5.3	33.2	FT^b + L^c	12.1	Brittle	35.9%; 21.3
6/S75-12-1500-d	–	3.8; 3.6	tilting	1.6	5.3	34.7	D^a+FT^b + L^c	12.4	Brittle	46.8%; 18.5
7/S75-15-1200-a	0.72	1.9; 2.9	tilting	2.2	7.0	66.4	D^a+FT^b + L^c	11.9	Brittle	58.1%; 27.8
9/S75-15-1200-d	–	1.4; 1.8	tilting	2.0	9.2	70.4	D^a+FT^b + L^c	10.5	Brittle	77.9%; 15.6
10/S75-15-1500-a	1.82	3.4; 3.2	tilting	2.3	5.4	50.8	D^a+FT^b + L^c	13.3	Brittle	54.1%; 23.3
12/S75-15-1500-d	–	3.7; 3.1	tilting	2.2	5.6	57.2	D^a+FT^b + L^c	14.9	Brittle	36.6%; 36.3
13/S100–12-1200-a	−0.73	1.0; 2.0	None	4.6	7.4	58.9	D^a+F^d + L^c	8.6	Brittle	29.5%; 41.5
14/S100–12-1200-c	–	4.8; 3.1	tilting	3.9	7.9	58.8	D^a+FT^b	8.9	Brittle	95.8%; 2.5
16/S100–12-1500-a	0.88	1.4; 1.3	tilting+ head-hearing	3.6	8.5	49.2	D^a+FT^b + L^c	9.0	Brittle	46.4%; 26.4
17/S100–12-1500-c	–	1.3; 1.4	None	3.5	7.4	51.9	D^a+FT^b + L^c	8.3	Brittle	70.7%; 15.2
18/S100–12-1500-d	–	3.1; 3.0	None	2.6	8.0	47.9	D^a+FT^b + L^c	11.5	Brittle	68.5%; 15.1
19/S100–20-1200-a	−1.38	1.2; 1.3	head shearing	5.6	11.5	123.1	D^a+FT^b	10.3	Brittle	87.7%; 15.1
20/S100–20-1200-c	–	2.9; 3.1	head shearing	3.0	11.1	115.2	D^a+FT^b + L^c	13.2	Brittle	57.6%; 48.8
21/S100–20-1200-d	–	2.4; 2.2	head shearing	4.3	11.5	126.3	D^a+FT^b	11.6	Brittle	76.9%; 29.2
22/S100–20-1500-a	−1.23	2.4; 1.9	head shearing	3.4	15.0	125.2	FT^b + L^c	11.7	Brittle	65.4%; 43.3
23/S100–20-1500-c	–	2.8; 2.7	head shearing	3.0	15.2	110.9	FT^b + L^c	16.0	Brittle	45.5%; 60.4
24/S100–20-1500-d	–	4.2; 1.8	head shearing	3.6	14.7	118.7	FT^b + L^c	13.0	Brittle	59.0%; 48.7
25/S100–30-1200-a	−1.55	1.4; 4.5	head shearing	7.2	17.4	211.9	FT^b + L^c	16.6	Brittle	37.1%; 133.2
26/S100–30-1200-c	–	0.6; 1.5	None	7.1	17.3	223.7	FT^b + L^c	12.8	Brittle	40.1%; 134
27/S100–30-1200-d	–	2; 1.8	head shearing	5.4	16.8	205.9	FT^b + L^c	13.6	Brittle	27.9%; 148.5
28/S100–30-1500-a	2.18	1.7; 1.5	None	3.0	20.2	188.9	F^d + FT^b + L^c	12.4	Brittle	20.7%; 149.8
29/S100–30-1500-c	–	5.3; 2.8	head shearing	5.7	20.6	199.3	F^d + FT^b + L^c	18.5	Brittle	32.3%; 134.9
30/S100–30-1500-d	–	1.4; 1.8	head shearing	3.1	20.9	213.3	F^d + FT^b + L^c	13.8	Brittle	33.1%; 142.7
31/S125–13-1200-a	–	0.2; 0.5	None	8.7	9.9	65.3	FT^b + L^c	6.7	Brittle	30.7%; 45.3
32/S125–13-1200-c	–	0.3; 0.7	None	4.4	9.9	61.7	FT^b + L^c	7.2	Brittle	33.3%; 41.2
33/S125–13-1200-d	−0.18	0.3; 0.2	None	4.5	9.9	64.7	FT^b + L^c	7.6	Brittle	43.5%; 36.6
34/S125–13-1500-a	−1.5	0.9; 0.96	None	3.1	9.7	65.2	FT^b + L^c	9.3	Brittle	52.4%; 31
35/S125–13-1500-c	–	0.8; 0.7	None	4.3	9.2	56.5	FT^b + L^c	8.7	Brittle	26.7%; 41.4
36/S125–13-1500-d	–	0.2; 0.5	None	3.0	9.9	63.2	FT^b + L^c	9.4	Brittle	45.6%; 34.4

Table 6 (*continued*)

Test no/ Specimen ID	Measured Initial eccentricity $e_{0,end}$ (mm)	Stud-to-track gap at top; bottom (mm)		Phase I		Phase II			Total axial shortening at the peak load, V_{BCT} (mm)	Phase III	
				Connection (S/T) screw failure type (visual observation)	Axial Stiffness k1 (kN/mm)	Axial stiffness k2,$_{BCT}$ (kN/mm)	Tested peak load, P_{uBCT} (kN)	Failure mechanism		Stud Failure type (visual observation)	Post-peak capacity reduction (% of ultimate capacity); reduced force (kN)
37/S125–20-1200-a	2.25	1.2;	1.9	None	4.5	14.7	144.9	FT[b] + L[c]	12.6	Brittle	56.1%; 63.6
38/S125–20-1200-c	–	3.9;	2.3	head shearing	4.3	14.8	150.0	FT[b] + L[c]	16.2	Brittle	47.3%; 79.1
39/S125–20-1200-d	–	2.5;	3.9	head shearing	3.8	14.3	152.0	FT[b] + L[c]	16.4	Brittle	78.4%; 32.8
40/S125–20-1500-a	−0.56	2.2;	1.9	head shearing	5.1	18.6	134.9	FT[b] + L[c]	11.7	Brittle	70.9%; 39.3
41/S125–20-1500-c	–	2.5;	1.3	head shearing	5.6	18.4	128.9	FT[b] + L[c]	11.5	Brittle	38.2%; 79.7
42/S125–20-1500-d	–	1.0;	1.9	head shearing	5.8	17.7	129.3	FT[b] + L[c]	10.8	Brittle	40.5%; 76.9

The test data corrupted for test no 8,11&15.

[a] D - distortional buckling;
[b] FT - Flexural torsional buckling;
[c] L - Local buckling;
[d] F - Flexural buckling about the minor axis;

Table 7
Experimental performance, failure mechanism, peak load, and post-peak behaviour of the studs in BCH.

Test No/ Specimen ID	Measured Initial eccentricity $e_{0,end}$ (mm)	Phase II				Phase III	
		Tested peak load, P_{UBCH} (kN)	Axial shortening at peak load, V_{BCH} (mm)	Axial stiffness, k2,$_{BCH}$ (kN/mm)	Failure mechanism	Stud Failure type (visual observation)	Post-peak capacity reduction (As a % age of the ultimate capacity); reduced capacity (kN)
43/S75-12-1200-b	0.81	36.4	4.0	9.5	F[d] + L[c]	Buckling	Gradual reduction.
44/S75-15-1200-b	−0.46	59.4	4.9	12.6	F[d] + L[c]	Buckling	Gradual reduction.
45/S100–12-1200-b	−4.37	29.8	3.8	8.0	FT[b] + D[a] + L[c]	Buckling	Gradual reduction.
46/S100–20-1200-b	−3.35	92.3	7.1	13.6	F[d] + D[a] + L[c]	Buckling	56.68%; 39.9 kN
47/S100–30-1200-b	−1.02	170.1	9.1	19.7	F[d] + D[a] + L[c]	Buckling	58.36%; 70.8 kN
48/S125–13-1200-b	0.1	60.5	5.9	12.0	F[d] + L[c]	Buckling	77.13%; 13.8 kN
49/S125–20-1200-b	0.46	128.0	8.1	17.2	F[d] + L[c]	Buckling	78.76%; 27.2 kN
50/S75-12-1500-b	−0.17	29.8	2.8	11.2	F[d] + L[c]	Buckling	Gradual reduction.
51/S75-15-1500-b	−0.17	43.8	3.7	13.3	F[d] + L[c]	Buckling	Gradual reduction.
52/S100–12-1500-b	0.71	43.9	4.2	11.6	F[d] + L[c]	Buckling	51.82%; 21.2 kN
53/S100–20-1500-b	3.57	86.6	5.3	18.9	F[d] + L[c]	Buckling	Gradual reduction.
54/S100–30-1500-b	0.07	140.2	6.1	24.3	F[d] + D[a] + L[c]	Buckling	Gradual reduction.
55/S125–13-1500-b	−0.22	42.7	3.7	13.0	F[d] + L[c]	Buckling	Gradual reduction.
56/S125–20-1500-b	−0.65	112.1	5.5	21.3	F[d] + L[c]	Buckling	Gradual reduction.

[a] D - distortional buckling;
[b] FT - Flexural torsional buckling;
[c] L - Local buckling;
[d] F - Flexural buckling about the minor axis;

hence, the web locally buckled at 50–60% of peak load, triggering the initial failure. All the studs experienced a sudden FT[b] + L[c] failure mechanism with an abrupt capacity reduction. The local web buckling concentrated near the mid-height at the peak load, forming a yield line. Local buckling of the lips was observed in the S125–13 but not in the S125–20 studs.
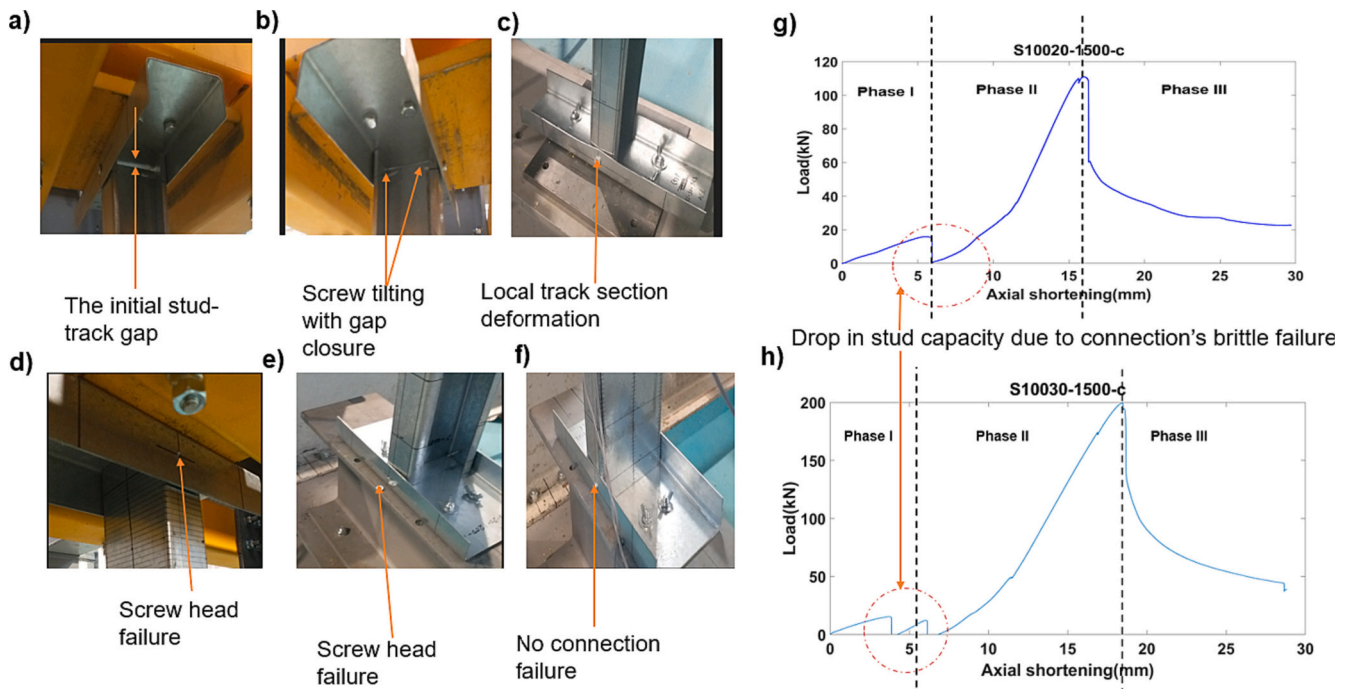
Fig. 6. Loading Phase I; a) initial stud-to-track gap, b) screw tilting failure in S75-12-1500-d, c) local track section deformation during gap closure and screw-tilting in S75-15-1500-d, d) & e) screw head failure in S100–12-1500-a & S125–20-1200-c, respectively f) no connection failure: S125–13-1200-d, and g) & h) drop in stud capacity.
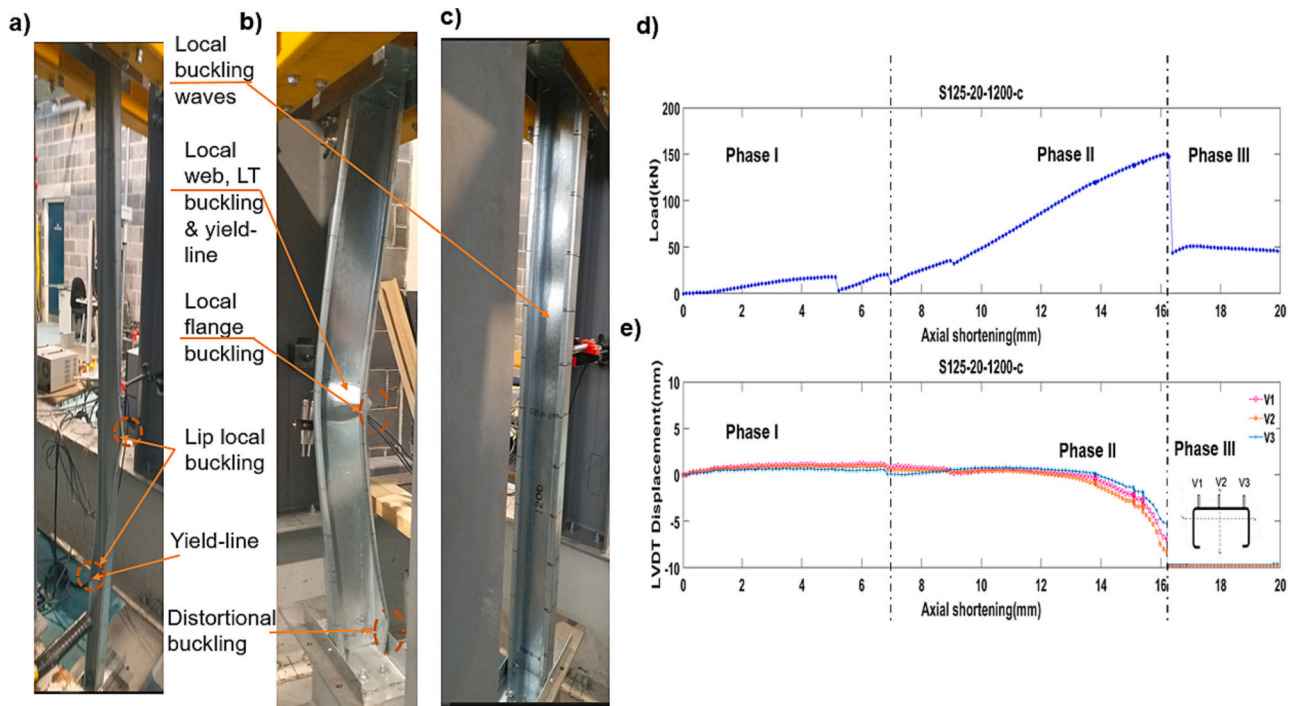

Fig. 7. Failure mechanisms at; a) S75-12-1500-d, b) S100–12-1500-d, c) S125–20-1200-c, d) load-axial shortening, and e) horizontal displacement-axial shortening for S125–20-1200-c.

3.1.2.1. Repeatability of results in Phase II. Table 6 and Fig. 8c demonstrate that the ultimate axial capacity of the studs and axial stiffness, $k2$, $_{BCT}$, obtained in repeated tests agreed reasonably well, with the low variation in the maximum axial load capacity (average 6.4%) and in $k2$, $_{BCT}$ (average 2.9%). The studs' maximum axial capacity decreased with the increase in both c_h/t and λ magnitude, as shown in Fig. 8a and b.

3.1.3. Phase III (BCT): Post-peak performance of the studs

After the studs reached their ultimate capacity, the load started decreasing as the failure was initiated. Although the percentage drop in stud capacity (Table 6) after the peak load varied for different samples, the studs' post-peak capacity reduction was closely related to the failure mode interactions. Whenever distortional buckling interacted with
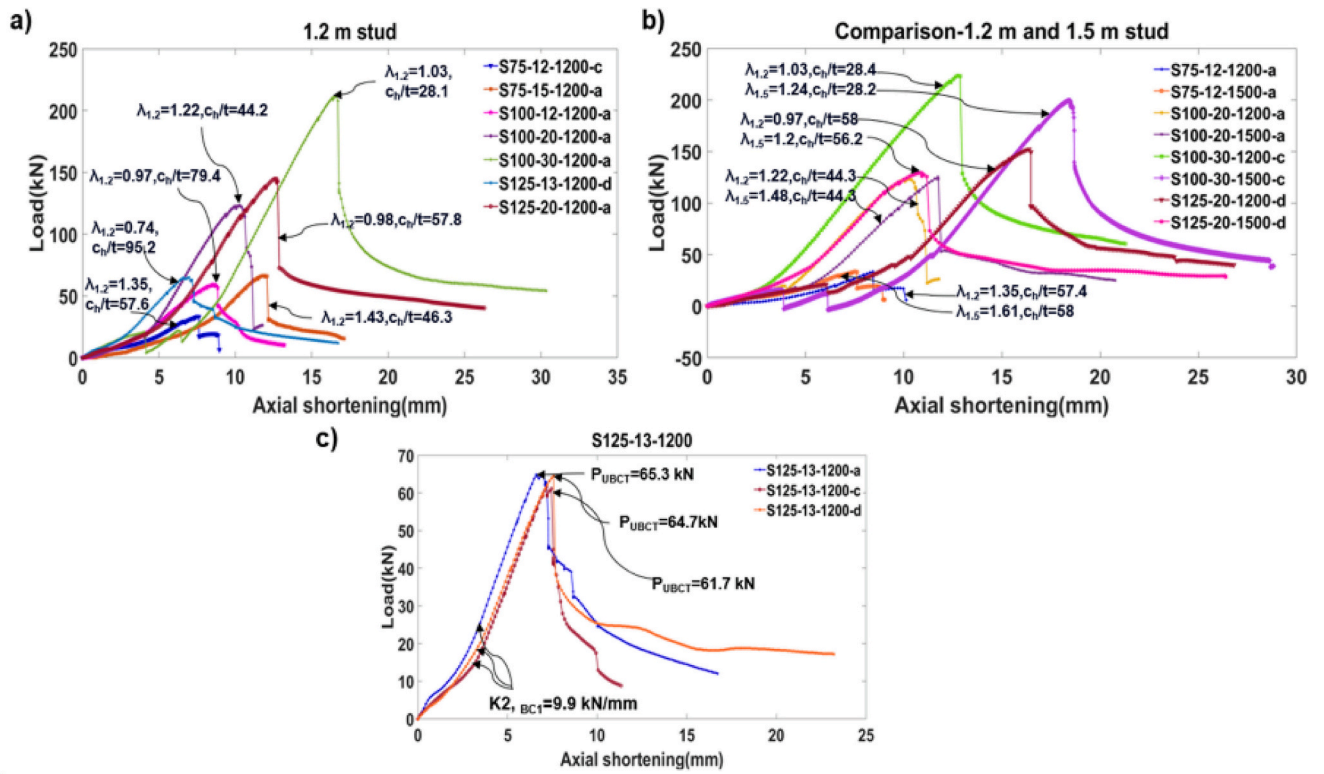
Fig. 8. Load-axial shortening response in BCT; a) all 1.2 m studs, b) 1.2 m and the corresponding 1.5 m studs, and c) example of the repeatability of the test results.

flexural-torsional buckling, there was a maximum decrease in the load-carrying capacity. The average capacity reduction of all the studs experiencing the $D^a + FT^b$ mechanism was 92.7%. The average drop in stud capacity in the complex $D^a + FT^b + L^c$ interaction was 59.5%. However, it varied widely, with a maximum of 87.7% for the S100–20-1200-a sample and a minimum of 35.9% for the S75-12-1500-c sample. The stud's capacity reduction after the peak varied in $FT^b + L^c$

interaction. Whenever flexural buckling occurred in the failure mechanism, the studs experienced a gradual failure, and the capacity reduction was the lowest, between 20% to 30% of the peak load.

3.1.4. Summary of BCT results

In loading Phase I, the studs' axial stiffness, $k1_{BCT}$, and axial compressive capacity were predominantly influenced by the non-linear
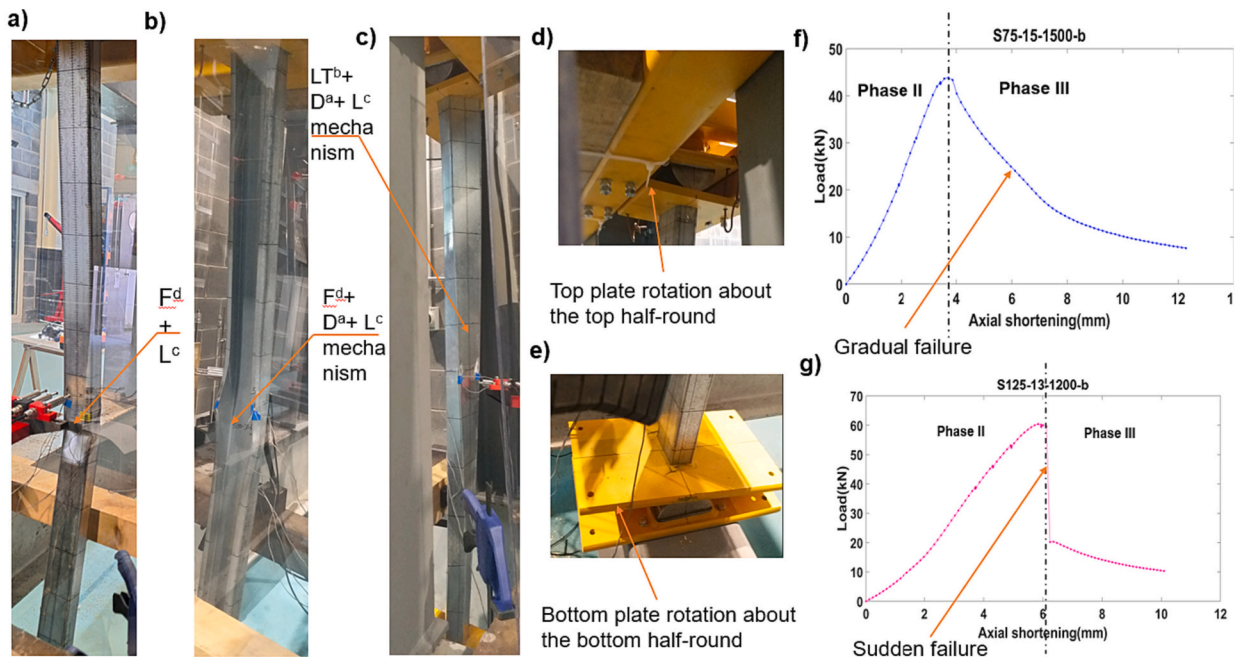

Fig. 9. Various failure mechanisms for BCH: a) S75-15-1500-b, b) S100–30-1200-b, c) S100–12-1200-b, d) & e) rotation of hinge assembly, and f) & g) load-axial shortening showing ductile and brittle failure, respectively.

connection stiffness, connection failure mechanism, and the stud-to-track gap. In loading Phase II, the tracks' warping rigidity dominated the studs' axial stiffness, k2$_{BCT}$, and the global failure (flexural-torsional buckling) mechanism. The complex interactions of various cross-sectional and global buckling modes were attributed to the closeness of critical buckling stress, a function of the studs' specific cross-sectional slenderness, member effective length, and boundary conditions. The distribution of geometric imperfections influenced the interaction of the global buckling modes. The competing buckling modes greatly affected the studs' post-peak capacity reduction in loading Phase III.

3.2. Test results for BCH

For BCH, the loading Phase I was absent, as there is no track section. The studs demonstrated a single axial stiffness up to the peak load. The studs' performance is described only in Phase II and Phase III. The peak load (P$_{uBCH}$), axial stiffness (k2, $_{BCH}$), and predominant failure mechanism of the studs in BCH are reported in Table 7. Fig. 9 shows the various failure mechanisms and load-axial shortening response of the selected samples tested under BCH, along with the top and bottom plate rotation about the half-round long-axis, demonstrating the hinge mechanism.

3.2.1. Phase II (BCH): Studs' performance up to the peak load

In BCH, the predominant global failure mode was flexural buckling about the minor centroidal axis. Most studs experienced the F^d + L^c interaction with a gradual reduction of studs' ultimate capacity. The studs with the lower c$_h$/t (S75 & S100) experienced flexural and local web buckling at 75–80% of the peak load. In the studs with higher c$_h$/t (S125), the failure was triggered by local web buckling, which gradually concentrated at the mid-height in the unloading path. The S100–30 and the 1.2 m S100–20 studs failed in the F^d + D^a + L^c mechanism, experiencing flexural and distortional buckling of the web-to-flange junction at 75–80% of the peak load, which concentrated at the mid-height at the ultimate load, along with local buckling of lips at the studs' mid-height. The S100–12-1200-b stud experienced a flexural torsional buckling failure mechanism due to the sample's higher initial twisting imperfection.

3.2.2. Phase III (BCH): Post-peak behaviour

Most studs undergoing the F^d + L^c mechanism experienced a gradual capacity reduction to over 50% of peak load (see Table 7), except for the 1.2 m S125 and 1.5 m S100–12 stud, which underwent a 50–78% sudden drop in the ultimate capacity (see Table 7). When the distortional buckling was involved, the studs experienced a 55–58% reduction of the ultimate load.

4. Discussion of test results

4.1. Comparison of the influence of boundary conditions BCT and BCH on studs' axial compressive performance

4.1.1. Ultimate capacity and evaluation of EC3 prediction

The average ultimate axial compressive capacity of the studs, tested with BCT (P$_{uBCT}$) and BCH (P$_{uBCH}$), is reported in Table 8. The maximum and minimum ultimate capacity ratios are presented in bold font. The stud's axial compressive capacity has also been calculated as per EC3 [11] in BCT & BCH (P$_{UECLBCT}$, P$_{UECLBCH}$), considering the stud's effective length, L, as the distance between the center of gravity of the half-rounds in BCH, and the distance between the top and bottom supporting plate in BCT. The studs' measured dimensions and material properties from the coupon test have been considered for P$_{UECL}$ calculation. Table 8 (Column 5) shows that the studs in BCT had, on average, 1.22 times higher axial compressive capacity than that in BCH. The higher capacity in BCT is caused by the warping rigidity provided by the track flanges at both ends of the studs. The higher axial compressive strength of individual studs with BCT, than in BCH will significantly influence the load redistribution mechanism and global structural behaviour of CFS panelised buildings, when the studs' are loaded beyond their elastic limit, especially under highly non-linear axial-compressive loading scenarios.

P$_{UBCT}$ is, on average, 1.8 times more than P$_{UECLBCT}$ (Table 8, Column 6), which demonstrates that the EC3 [11] EWM, with an E$_L$ of 1, predicts a highly conservative axial capacity of the studs in BCT. As per EC3 EWM, the E$_L$ that accurately predicted the studs' tested axial compressive strength was determined and presented in Table 8, Column 8, and discussed further in Section 4.2. P$_{UBCH}$ is, on average, 1.5 times (Table 8, Column 7) more conservative than P$_{UECL}$, which approximately agreed with previous research [17,18] on hinged boundary conditions. The P$_{UECL}$ was also calculated against the nominal material strengths of respective steel grades, presented in Table 4, and the negligible difference was observed in the results, presented in Table 8, as the measured strength was not significantly higher than the nominal strength (discussed in Section 2.4.).

4.1.2. Axial stiffness

Table 9 compares the studs' axial stiffness in BCT and BCH.

The maximum and minimum stiffnesses are shown in bold font. Column 5 in Table 9 demonstrates that, in Phase II, the BCT caused a 30% lower axial stiffness than that in the BCH (k2, $_{BCTavg}$ is 0.7 times k2,

Table 8
Comparison of studs' ultimate capacity in BCT (averaged) and BCH.

Specimen	P$_{uBCT}$ (kN)	P$_{uBCH}$ (kN)	P$_{UECL,BCT}$ (kN)	P$_{UECL,BCH}$ (kN)	P$_{uBCT}$/P$_{uBCH}$	P$_{uBCT}$/P$_{uECL,}$ BCT	P$_{uBCH}$/P$_{uECL,BCH}$ [7]	ELF$_{EC3}$
			[3]	[4]	[5]	[6]		
	[1]	[2]						[8]
S75-12-1200	36.0	36.4	19.4	19.3	**0.99**	1.9	1.9	0.58
S75-12-1500	33.7	29.8	14.6	13.7	1.13	**2.3**	**2.2**	0.5
S75-15-1200	68.4	59.4	31.7	31.8	1.15	2.2	1.9	0.46
S75-15-1500	54.0	43.8	24.1	24	1.23	2.2	1.8	0.58
S100–12-1200	58.9	29.8	33.5	31	**1.97**	1.8	1	0.35
S100–12-1500	49.7	44.0	26	24.8	1.13	1.9	1.8	**0.33**
S100–20-1200	121.6	92.3	75.6	70.6	1.32	1.6	1.3	0.58
S100–20-1500	118.3	86.6	56.9	53.9	1.37	2.1	1.6	0.49
S100–30-1200	213.8	170.0	148.2	141.6	1.26	1.4	1.2	0.5
S100–30-1500	200.5	140.2	118.6	113.3	1.43	1.7	1.2	0.5
S125–13-1200	63.9	60.5	54.7	53.3	1.06	**1.2**	1.1	0.62
S125–13-1500	61.6	42.7	47.9	46.5	**1.44**	1.3	**0.9**	**0.64**
S125–20-1200	149.0	128.0	103.4	98.6	1.16	1.4	1.3	0.48
S125–20-1500	131.0	112.1	82.5	80.9	1.17	1.6	1.4	0.59
Mean					1.22	1.8	1.5	0.5
Standard deviation (SD)					0.14	0.4	0.4	0.1

Table 9
Comparison of the studs' experimental axial stiffness in BCT (averaged) and BCH.

Specimen	BCT		BCH	ratio		
	$k1_{BCT,avg}$ (kN/mm)	$k2_{,BCTavg}$ (kN/mm)	$k2_{,BCH}$ (kN/mm)	$k2_{,BCTavg}$ / $k1_{BCT,avg}$ [4]	$k2_{,BCTavg}$/ $k2_{,BCH}$	$K1_{,BCTavg}$/ $k2_{,BCH}$
	[1]	[2]	[3]		[5]	[6]
S75-12-1200	2.68	6.00	9.50	2.24	0.63	0.28
S75-12-1500	**1.72**	**5.30**	11.17	3.08	0.47	**0.15**
S75-15-1200	2.12	8.09	12.56	3.81	0.64	0.17
S75-15-1500	2.24	5.50	13.26	2.45	**0.41**	0.17
S100–12-1200	4.24	7.64	**8.00**	1.80	**0.96**	**0.53**
S100–12-1500	3.25	7.94	11.61	2.44	0.68	0.28
S100–20-1200	4.32	11.37	13.58	2.63	0.84	0.32
S100–20-1500	3.35	14.98	18.90	4.48	0.79	0.18
S100–30-1200	**6.54**	17.18	19.71	2.62	0.87	0.33
S100–30-1500	3.92	**20.58**	24.32	5.25	0.85	0.16
S125–13-1200	5.85	9.86	12.02	**1.69**	0.82	0.49
S125–13-1500	3.46	9.62	12.96	2.78	0.74	0.27
S125–20-1200	4.18	14.62	17.24	3.50	0.85	0.24
S125–20-1500	5.50	18.25	21.34	3.32	0.86	0.26
Mean				3.01	0.7	0.27
Standard deviation				1.00	0.16	0.12

$_{BCH}$). Also, from Table 9, Column 4, in BCT, the studs' Phase II axial stiffness, $k2$, $_{BCTavg}$, was three times higher than the Phase I stiffness, $k1_{BCT,avg}$, which is reasonable as $k1_{BCT,avg}$ represents only the non-linear shear stiffness of the connection until the closure of the stud-to-track gap. Such two-stage axial stiffness behaviour of individual studs with BCT, particularly the lower Phase II axial stiffness in BCT, than in BCH will significantly influence the load redistribution mechanism and global structural behaviour of CFS panelised buildings, when the studs' are loaded beyond their elastic limit, especially under highly non-linear axial compressive loading scenarios.

4.1.3. Axial shortening, out-of-plane deflection at the studs' mid-height at peak load

Column 8 in Table 10 shows that until the peak load, the total axial shortening in BCT (V_{BCT}) was 2.3 times higher than that in BCH (V_{BC2}). Columns 9 and 10 show that in BCT, 30% of the total axial shortening (up to peak load) happened in Phase I, while the remaining 70% occurred in Phase II. Column 11 signifies that in BCT, even excluding the gap displacement ($V_{BCTPhase I}$), the warping rigidity of the tracks caused 70% higher axial shortening of studs until peak load in Phase II than that

in BCH. The studs' significantly higher (70%) Phase II axial shortening in BCT than in BCH will substantially influence the load redistribution mechanism and global structural behaviour of CFS panelised buildings when the studs' are loaded beyond their elastic limit, especially under highly non-linear axial compressive loading scenarios. No trend was observed in the magnitude of the studs' mid-height horizontal deflection due to the change in the boundary condition; the studs' effective length governed it. On average, the 1.5 m studs underwent two times higher out-of-plane deflection at the webs' mid-depth and corner locations than the 1.2 m studs.

4.1.4. Predominant global failure mechanism and studs' axial compressive strain

The axial compressive strain was closely correlated with the studs' predominant global failure mechanism in BCT and BCH. The global flexural buckling failure mode in BCH caused on average, 58% higher axial compressive strain, particularly at the studs' web at mid-height, than that caused by the flexural torsional mode in BCT. The studs web's higher axial compressive strain in BCT than in BCH is visible in Fig. 10 in the load versus strain plot of S125–20-1500 and S75–15 -

Table 10
Comparison of studs' axial shortening in BCT (averaged) and BCH.

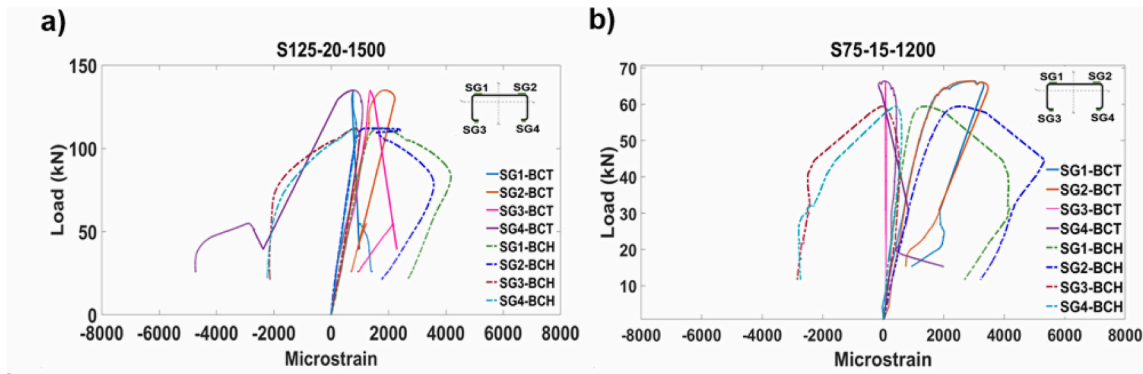| Specimen	V_{BCT} Phase I,avg. (mm)	$V_{BCT\_}$ Phase II,avg. (mm)	V_{BCT}(mm)				V_{BCH} (mm)	Ratio			
			Max	Min	Avg	Std Dev._ $V_{BCT,}$ avg.		$V_{BCT,}$ $_{avg}$/ V_{BCH}	$V_{BCT\_}$ PhaseI, $_{avg}$/ $V_{BCT,}$ avg.	$V_{BCT\_}$ PhaseII, $_{avg}$/ $V_{BCT,}$ avg.	$V_{BCT\_}$ PhaseII, $_{avg}$/ V_{BCH}
	[1]	[2]	[3]	[4]	[5]	[6]	[7]	[8]	[9]	[10]	[11]
S75-12-1200	1.8	5.9	8.0	7.6	7.8	0.2	4.0	1.9	0.24	0.76	1.5
S75-12-1500	2.0	9.0	12.4	8.4	11.0	2.2	**2.8**	**4.0**	0.19	0.81	3.2
S75-15-1200	1.9	9.4	11.9	10.5	11.2	1	4.9	2.3	0.17	0.83	1.9
S75-15-1500	2.5	11.6	14.9	13.3	14.1	1.1	3.7	3.8	0.18	0.82	3.1
S100–12-1200	2.8	6	8.9	8.6	8.8	0.2	3.8	2.3	0.32	0.68	1.6
S100–12-1500	2.3	7.3	11.5	8.3	9.6	1.7	4.2	2.3	0.24	0.76	1.7
S100–20-1200	4.1	7.6	13.2	10.3	11.7	1.5	7.1	1.6	0.36	0.64	1.1
S100–20-1500	5.2	8.4	16.0	11.7	13.6	2.2	5.3	2.6	0.39	0.61	1.6
S100–30-1200	4.3	10.0	16.6	12.8	14.3	2	**9.1**	1.6	0.29	0.71	1.1
S100–30-1500	4	10.9	**18.5**	12.4	14.9	3.2	6.1	2.5	0.26	0.74	1.8
S125–13-1200	2	5.1	16.4	**6.7**	7.2	0.5	5.9	**1.2**	0.28	0.72	0.9
S125–13-1500	3.3	5.8	9.4	8.7	9.1	0.4	3.7	2.5	0.36	0.64	1.6
S125–20-1200	4.7	10.4	16.4	12.6	15.1	2.1	8.1	1.9	0.31	0.69	1.3
S125–20-1500	4.9	6.5	11.7	10.8	11.3	0.4	5.5	2.1	0.43	0.57	1.2
Mean								2.3	0.3	0.7	1.7
Standard deviation(Std Dev)								0.8	0.08	0.08	0.7

Fig. 10. Comparison of studs' axial compressive strains in BCT and BCH: a) S125–20-1500 and b) S75-15-1200.

1200 studs. This behaviour signifies that the studs experienced delayed material yielding and, therefore, delayed failure due to the lower axial-compressive strain at the stud web caused by the beneficial effects of the tracks' warping rigidity under BCT compared to BCH. The studs web's significantly lower (58%) axial compressive strain in BCT than in BCH will substantially influence the load redistribution mechanism and global structural behaviour of CFS panelised buildings when the studs' are loaded beyond their elastic limit, especially under highly non-linear axial compressive loading scenarios.

4.1.5. Restraint stiffness of BCT compared to the BCH

The 22% higher axial compressive capacity (as discussed in Section 4.1.1, Column 5, Table 8) of the studs with BCT compared to BCH is caused by the warping or moment fixity of the track boundary condition. The BCH has zero moment fixity against rotation. However, with BCT, under axial compressive loading, the studs tend to rotate about their edge at the end of the cross-section, leading to the generation of a restoring moment, $M_R = 0.5P_uh$ (P_u being the axial compressive load and h being the cross-section depth) [14]. At low levels of axial load (P_U), M_R is low, and the boundary condition is approximately pinned. With the increase in P_U, M_R increases, causing increased end fixity [14]. Similarly, increasing the studs' cross-sectional depth, h, for deeper members causes higher M_R, while lower M_R is generated for shallower members. Higher end fixity or higher restraint stiffness causes the studs to achieve higher axial compressive capacity with BCT. Such behaviour is observed in the results of this study (Column 5, Table 8) and also by others [7,14]. Several other factors, such as the non-linear connection stiffness and stud-to-track gap, can influence M_R. The restraint stiffness caused by BCT can be quantified for various studs by dividing the restoring moment, M_R, by the rotation at the end of the stud cross-section about the stud edge. In this study, the rotation at the end of

the stud cross-section about the edge of the stud was not measured; hence the accurate restraining stiffness provided by the BCT could not be quantified for various stud cross-sections. However, the effect of the restraint stiffness offered by the BCT has been investigated further to quantify an accurate, effective length factor (E_L) for the studs that can be used to predict their safe and optimal axial compressive capacity under BCT. This is discussed further in Section 4.2.

4.1.6. The overall influence of BCT on the efficient design of studs as compared to BCH

In practice, studs in CFS wall panels are designed to resist axial compression, considering a pin-ended boundary condition (BCH), due to lack of design guidance to assess the precise effect of the real-world track boundary condition (BCT). This experimental investigation and comparison of test results under BCT and BCH revealed a significant difference in the studs' axial-compressive performance and failure mechanisms under these boundary conditions, as summarised in Fig. 11.

In BCT, the presence of the stud-to-track gap and non-linear shear stiffness of the S/T screw caused the axial stiffness of the stud-track assembly to be significantly lower until the closure of the gap, (on average) 30% of the axial stiffness in BCH. After the gap closed, although the studs achieved 20% higher ultimate capacity in BCT than in BCH, the studs' axial stiffness in BCT was only 70% of that in BCH. This caused the studs to undergo 70% higher axial shortening post-gap closing until the peak load (Phase II) in BCT than in BCH. Furthermore, a brittle connection failure happened in BCT for the thicker gauge studs, and the studs completely lost their capacity for a point in time until the stud-to-track gap was fully closed. In addition, the comparison of the axial compressive strain results in BCT & BCH (Fig. 10) revealed that the global flexural buckling failure mechanism caused earlier material yielding and stud failure in BCH than in BCT. Combining all these
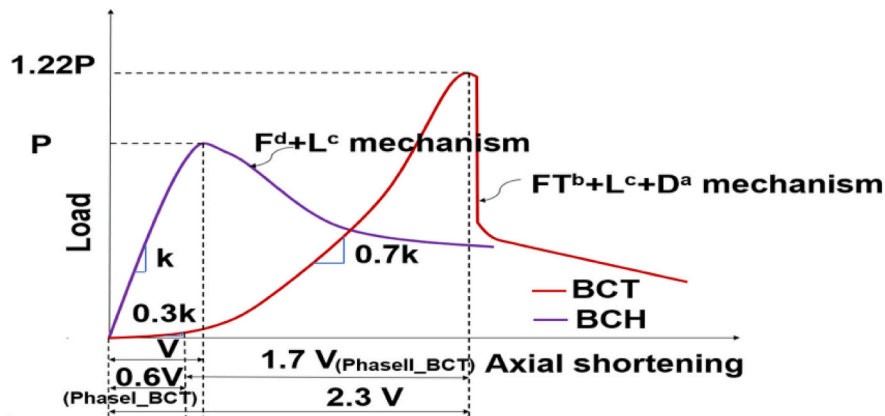

Fig. 11. Schematic of the comparison of studs' axial compressive performance in BCT and BCH.

effects, in BCT, the individual stud's axial compressive performance will significantly influence the load redistribution mechanism and global structural behaviour of CFS panelised buildings when- loaded beyond their elastic limit. Hence, it is recommended that, along with the higher ultimate strength, practitioners must consider the two-stage lower axial stiffness and higher axial shortening, complex local-distortion-flexural torsional buckling failure mechanism, for the efficient design of studs, in CFS wall panels, especially when subjected to highly non-linear axial compressive loading scenarios.

4.2. Estimation of the effective length factor (E_L) as per EC3

According to Table 8, the EC3 [11] design method with $E_L = 1$ predicted 80% lower axial compressive strength of the studs in BCT. For the studs' optimal design in BCT, it is necessary to establish an E_L that can closely predict the studs' higher axial compressive strength. Based on EC3 calculations, the E_L that accurately predicted the studs' tested axial compressive strength was determined and presented in Table 8, Column 8. The results show that the maximum and minimum E_L are 0.64 for S125–13-1500 and 0.33 for S100–12-150 studs, respectively. The average of all E_L is 0.5, with a standard deviation of 0.1. Based on these results, an upper bound estimate of the E_L was determined by adding the mean E_L (0.5) with one standard deviation (0.1), i.e., $0.5 + 0.1 = 0.6$, which is close to the maximum E_L 0.64 obtained in this study. Hence, a safe E_L of 0.65 was considered to predict the studs' axial compressive strength in BCT. In Fig. 12, the tested strength P_{UBCT} and EC3 predicted strength for E_L 0.65 and 1 ($P_{UEC0.65L}$ and P_{UECL}, respectively) normalized by EC3 cross-section compression resistances $A_{eff}f_y$, (A_{eff} is the effective cross-sectional area in compression, f_y is 0.2% proof strength from coupon test data) are plotted against corresponding non-dimensional slenderness ratios ($\lambda_{0.65L}$ for P_{UBCT} & $P_{UEC0.65L}$, λ_L for P_{UECL}) and the studs' strength curves for the EC3 predicted strengths are generated. Fig. 12 shows that the tested strengths in BCT are much higher than the P_{UECL} strength but closer to the $P_{UEC0.65L}$ strength. Hence, when EC3 EWM is adopted, an E_L 0.65 is suggested to obtain an optimal prediction of the CFS studs' axial compressive strength in BCT, with No 12 S/T screws used as the stud-to-track connections.

5. Conclusions

The axial compressive performance of bare CFS-lipped channel sections used as studs was investigated for the first time under real-world track boundary conditions (denoted as BCT), considering the combined effect of the tracks warping rigidity, stud-to-track gap, semirigid

connection stiffness, and various cross-sectional slenderness. All existing testings on bare CFS studs have employed ideal hinged (BCH) and fixed boundary conditions or else the BCT for sheathed stud-wall panels only. An experimental program was conducted on 42 industry-standard CFS-lipped channel sections of five different thicknesses (1.2–3 mm), three depths (75,100, & 125 mm), and two heights: 1.2 m & 1.5 m with BCT. An additional 14 studs, having cross-sections and heights identical to those in BCT, were tested with BCH as a comparator to BCT. Displacement-controlled static concentric axial compressive loading was applied to the studs with BCT and BCH. Material properties (e.g., Young's modulus), geometric imperfections, and initial out-of-plane eccentricities of the studs were measured in detail. The test results demonstrated that the track-boundary condition significantly influenced the studs' axial compressive performance and failure mechanism, as summarised below:

- **Ultimate axial compressive capacity:** On average, the studs in BCT achieved 1.22 times higher ultimate axial compressive capacity than in BCH due to the warping fixity provided by the tracks in BCT.
- **Axial stiffness:** A two-stage axial stiffness was observed in BCT, Phase I stiffness until the closure of the stud-to-track gap and Phase II stiffness after the gap closure up to the peak load. In contrast, a single axial stiffness was observed in BCH until the peak load due to the non-existence of the gap. The axial stiffness in BCT, post-gap closure, was 70% of that in BCH.
- **Axial shortening:** On average, the axial shortening of the BCT-tested studs was 2.3 times higher than that of BCH-tested studs until peak load.
- **Global failure mechanism:** BCT triggered the studs' global flexural torsional buckling failure mechanism instead of the flexural buckling failure mechanism in BCH.
- **Axial compressive strain**: Under BCT and BCH, the studs' global buckling failure mechanism dominated their axial-compressive strain behaviour. On average, the global flexural buckling failure mode in BCH caused 58% higher axial compressive strain, particularly at the studs' web at mid-height, than that caused by the flexural torsional mode in BCT.

The studs' post-peak axial capacity reduction in BCT and BCH was closely correlated with the interaction of various global and cross-sectional buckling modes. Whenever the distortional buckling interacted with other buckling modes, the studs underwent the highest capacity reduction, 92.7% in BCT and 58% in BCH.

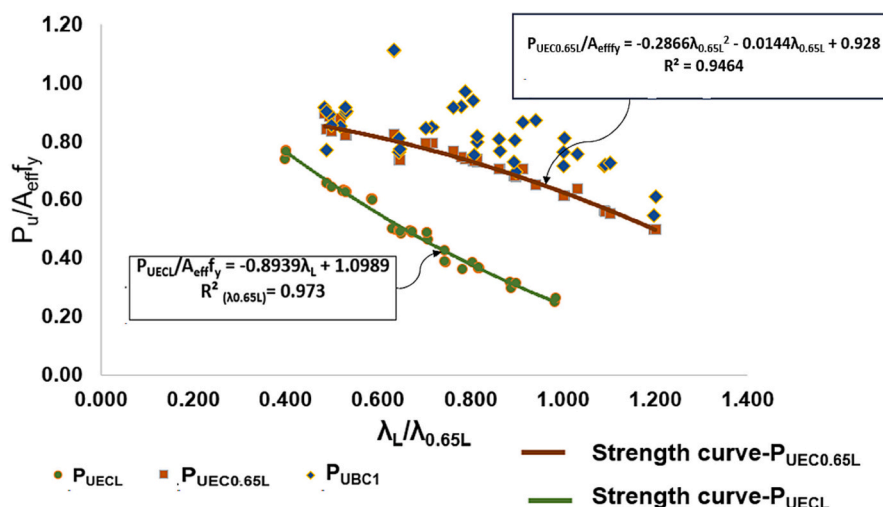An effective length factor (E_L) of 0.65 was suggested instead of E_L 1

Fig. 12. Comparison of test and EC3 failure loads considering E_L 0.65 & 1.

to optimally predict the studs' axial compressive strength in BCT using the EC3 effective width method. It was also recommended that along with the higher axial compressive strength, practitioners must consider the lower two-stage axial stiffness and higher axial shortening of studs under BCT for the studs' efficient design. Since the individual stud's performance under these combined effects significantly influences the load redistribution mechanism and the global structural behaviour of CFS panelised buildings, especially when the studs are loaded beyond their elastic limit under highly non-linear axial-compressive loading scenarios.

CRediT authorship contribution statement

Sohini Mishra: Writing – review & editing, Writing – original draft, Validation, Software, Project administration, Methodology, Investigation, Formal analysis, Data curation, Conceptualization. **Ciaran McNally:** Writing – review & editing, Supervision, Resources, Project administration. **Andrzej M. Wrzesien:** Resources, Investigation, Funding acquisition. **Daniel P. McCrum:** Writing – review & editing, Supervision, Resources, Project administration, Funding acquisition, Conceptualization.

Declaration of competing interest

The authors declare that they have no known competing financial interests or personal relationships that could have appeared to influence the work reported in this paper.

Data availability

The data that has been used is confidential.

Acknowledgment

References

[1] I. Papargyriou, I. Hajirasouliha, J. Becque, K. Pilakoutas, Performance-based assessment of CFS strap-braced stud walls under seismic loading, J. Constr. Steel Res. 183 (2021) 106731.

[2] J. Lim, D. Nethercot, Design and development of a general cold-formed steel portal framing system, Struct. Eng. 80 (21) (2002) 31–39.

[3] A. Davies, Modern Methods of Construction a Forward-Thinking Solution to the Housing Crisis, RICS, London, 2018.

[4] X. Dai, Numerical Modelling and Analysis of Structural Behaviour of Wall-Stud Cold-Formed Steel Shear Wall Panels under in-Plane Monotonic Loads, 2012.

[5] K.D. Peterman, B.W. Schafer, Sheathed cold-formed steel studs under axial and lateral load, J. Struct. Eng. 140 (10) (2014).

[6] F. Yilmaz, S.M. Mojtabaei, I. Hajirasouliha, J. Becque, Behaviour and performance of OSB-sheathed cold-formed steel stud wall panels under combined vertical and seismic loading, Thin-Walled Struct. 183 (2023) 110419.

[7] L.C.M. Vieira, Y. Shifferaw, B.W. Schafer, Experiments on sheathed cold-formed steel studs in compression, J. Constr. Steel Res. 67 (10) (2011) 1554–1566.

[8] R.M. Lawson, A.G.J. Way, M. Heywood, J.B.P. Lim, R. Johnston, K. Roy, Stability of light steel walls in compression with plasterboards on one or both sides, Proc. Insti. Civil Eng. Struct. Build. 173 (6) (2020) 394–412.

[9] H.S. Pham, C.D. Moen, Stiffness and Strength of Single Shear Cold-Formed Steel Screw-Fastened Connections, 2015.

[10] R.A. LaBoube, P.F. Findlay, Wall stud-to-track gap: experimental investigation, J. Archit. Eng. 13 (2) (2007) 105–110.

[11] CEN, EN1993-1-3 Eurocode 3: Design of Steel Structures, Part 1.3: Supplementary Rules for Cold Formed Members and Sheeting, European Committee for Standardization, Brussels, 2006.

[12] AISI, North American Cold-Formed Steel Specification: Specification for the Design of Cold-Formed Steel Structural Members, American Iron and Steel Institute, Washington, DC, USA, 2001.

[13] Y. Telue, M. Mahendran, Numerical modelling and design of unlined cold-formed steel wall frames, J. Constr. Steel Res. 60 (8) (2004) 1241–1256.

[14] C. Kyprianou, P. Kyvelou, L. Gardner, D.A. Nethercot, Experimental study of sheathed cold-formed steel beam–columns, Thin-Walled Struct. 166 (2021) 108044.

[15] B. Young, K.J. Rasmussen, Tests of fixed-ended plain channel columns, J. Struct. Eng. 124 (2) (1998) 131–139.

[16] J. Becque, The Interaction of Local and Overall Buckling of Cold-Formed Stainless Steel Columns, Ph.D. thesis, The University of Sydney, 2008.

[17] M. Peiris, M. Mahendran, Behaviour of cold-formed steel lipped channel sections subject to eccentric axial compression, J. Constr. Steel Res. 184 (2021).

[18] J. Ye, I. Hajirasouliha, J. Becque, Experimental investigation of local-flexural interactive buckling of cold-formed steel channel columns, Thin-Walled Struct. 125 (2018) 245–258.

[19] J.S. Rajkannu, S.A. Jayachandran, Flexural-torsional buckling strength of thin-walled channel sections with warping restraint, J. Constr. Steel Res. 169 (2020).

[20] J. Ye, R. Feng, W. Chen, W. Liu, Behavior of cold-formed steel stud with sheathing subjected to compression, J. Constr. Steel Res. 116 (2016) 79–91.

[21] H. Wu, S. Chao, T. Zhou, Y. Liu, Cold-formed steel framing walls with infilled lightweight FGD gypsum Part II: Axial compression tests, Thin-Walled Struct. 132 (2018) 771–782.

[22] C. Sonkar, D.P. McCrum, Axial compressive behaviour of cold-formed steel single-stud wall panels with one-sided sheathing and two-sided dissimilar sheathing board configurations: experimental and analytical study, Thin-Walled Struct. 187 (2023) 110733.

[23] F.J. Meza, J. Becque, I. Hajirasouliha, Experimental study of the cross-sectional capacity of cold-formed steel built-up columns, Thin-Walled Struct. 155 (2020) 106958.

[24] CEN, EN1993-1-1 Eurocode3: Design of Steel Structures, Part 1.1: General Rules and Rules for Buildings, European Committee for Standardization, Brussels, 2005.

[25] BS EN ISO 6892-1:2019, Metallic materials - Tensile testing. Method of test at room temperature, Geneva, Switzerland, 2019.

[26] BS EN 10346, Continuously hot-dip coated steel flat products for cold forming — Technical delivery conditions, 2015.

[27] D. Camotim, A.D. Martins, P.B. Dinis, B. Young, M.T. Chen, A. Landesmann, Mode interaction in cold-formed steel members: state-of-art report, ce/papers 4 (2–4) (2021) 34–64.

[28] V. Zeinoddini, B. Schafer, Simulation of geometric imperfections in cold-formed steel members using spectral representation approach, Thin-Walled Struct. 60 (2012) 105–117.

[29] B.W. Schafer, T. Peköz, Computational modeling of cold-formed steel: characterizing geometric imperfections and residual stresses, J. Constr. Steel Res. 47 (3) (1998) 193–210.

[30] ASTM, Standard Specification for Installation of Load Bearing Transverse and Axial Steel Studs and Related Accessories, ASTM C 1007, West Conshohocken, Pa, 2004.